Lawrence Berkeley National Laboratory
LBL Publications

Title

Engineering Supramolecular Hybrid Architectures with Directional Organofluorine Bonds.

Permalink

https://escholarship.org/uc/item/3z908739

Journal

Small Science, 4(1)

Authors

Kotei, Patience
Paley, Daniel
Oklejas, Vanessa
et al.

Publication Date

2024

DOI

10.1002/smsc.202300110

Peer reviewed

eScholarship.org Powered by the California Digital Library
University of California

Author Manuscript
Author Manuscript
Author Manuscript
Author Manuscript

HHS Public Access
Author manuscript
Small Sci. Author manuscript; available in PMC 2025 January 31.

Published in final edited form as:
Small Sci. 2024 January ; 4(1): . doi:10.1002/smsc.202300110.

Engineering Supramolecular Hybrid Architectures with Directional Organofluorine Bonds

Patience A. Kotei[1,2], **Daniel W. Paley**[3], **Vanessa Oklejas**[3], **David W. Mittan-Moreau**[3], **Elyse A. Schriber**[1,2], **Mariya Aleksich**[1,2], **Maggie C. Willson**[1,2], **Ichiro Inoue**[6], **Shigeki Owada**[6,7], **Kensuke Tono**[6,7], **Michihiro Sugahara**[6], **Satomi Inaba-Inoue**[7,8], **Andrew Aquila**[4], **Frédéric Poitevin**[4], **Johannes P. Blaschke**[5], **Stella Lisova**[4], **Mark S. Hunter**[4], **Raymond G. Sierra**[4], **José A. Gascón**[2], **Nicholas K. Sauter**[3], **Aaron S. Brewster**[3], **J. Nathan Hohman**[1,2]

[1]Institute of Materials Science, University of Connecticut, CT, 06269, USA

[2]Department of Chemistry, University of Connecticut, CT, 06269, USA

[3]Molecular Biophysics and Integrated Bioimaging Division, Lawrence Berkeley National Laboratory, Berkeley, CA, 94720, USA

[4]Linac Coherent Light Source, SLAC National Accelerator Laboratory, Menlo Park, CA, 94025, USA

[5]National Energy Research Scientific Computing Center, Lawrence Berkeley National Laboratory, Berkeley, CA, 94720, USA

[6]RIKEN SPring-8 Center, 1-1-1 Kouto, Sayo, Hyogo 679-5148, Japan

[7]Japan Synchrotron Radiation Research Institute, 1-1-1 Kouto, Sayo, Hyogo 679-5198, Japan

[8]Structural Biology Research Center, Photon Factory, Institute of Materials Structure Science, High Energy Accelerator Research Organization, 1-1 Oho, Tsukuba, Ibaraki, 305-0801, Japan

Abstract

Understanding how chemical modifications alter the atomic-scale organization of materials is of fundamental importance in materials engineering and the target of considerable efforts in computational prediction. Incorporating covalent and non-covalent interactions in designing crystals while “piggybacking” on the driving force of molecular self-assembly has augmented our efforts to understand the emergence of complex structures using directed synthesis. Here, we prepared microcrystalline powders of the silver 2-, 3-, and 4-fluorobenzenethiolates and resolved their structures by small molecule serial femtosecond X-ray crystallography (smSFX). These three compounds enable us to examine the emergence and role of supramolecular synthons in the crystal structures of three-dimensional metal-organic chalcogenolates (MOChas). The unique divergence in their optoelectronic, morphological, and structural behavior was assessed. The extent of C-H···F interactions and their influence on the structure and the observed trends in the thermal stability of the crystals were quantified through theoretical calculations and thermogravimetric analysis.

Conflict of Interest
Authors declare no competing interests.

Author Manuscript Author Manuscript Author Manuscript Author Manuscript

Keywords

Metal-Organic Chalcogenolates; C-F bonding; smSFX; Supramolecular Synthons; Crystal Engineering

Synthons are highly conserved supramolecular patterns that emerge in crystal structures of related molecules. [1,2] Synthons enable the classification of recurring patterns for crystal engineering because they give a systematic approach to understanding how different molecules self-organize. [3,4] The rise of hybrid architectures such as metal-organic chalcogenolates (MOChas) that yield well-defined and highly inter-related supramolecular and coordinated phases present an opportunity to examine the roles played by synthons in the emergence of inorganic structure in complex materials. However, it has been challenging to relate compatible synthons to inorganic structures because the small crystal sizes endemic to MOChas make structural solutions challenging to acquire. We have recently demonstrated that small-molecule serial femtosecond crystallography (smSFX) is useful for accelerating the characterization of compounds in this material class. [5] Here, we use this approach to perform microcrystallography on the three silver fluorobenzenethiolates. Each isomer yields distinct crystal Bravais lattice, spacegroup, and habit. The detailed structures reveal how the patterns of CF-H hydrogen bonding relate to the inorganic nanostructures in the context of the alignments and energies of the interactions of the supramolecular phase. These structures reveal C-H···F hydrogen bonding and its role in modulating the inorganic structures. The interaction strengths are evaluated in the context of material thermal stability. Because fluorine is isosteric with hydrogen, [6] we can examine the role of the dipolar interactions largely in isolation of steric factors in MOChas. [7,8] We identify compatibilities between organic synthons and the resulting inorganic architectures and conclude with a discussion of the supramolecular synthons that coexist with the low-dimensional inorganic structure. This work provides a foundation for a systematic approach to the reticular design of hybrid materials with both supramolecular and inorganic components.

The MOChas are self-assembling hybrid materials that form 0-dimensional complexes and clusters, 1-dimensional polymers, and 2-dimensional sheets depending on the steric demands of the organic ligands. [8] These compounds have recently attracted interest for excitonic photophysical properties expressed as their bulk 3-dimensional crystals. [9–12] This unique arrangement of monolayer performance in 3D crystals and numerous opportunities for crystal engineering by metal, [13] chalcogen, [14,15] and ligand (organic group) substitution makes the system an ideal test platform for understanding the emergence of complex/function properties in hybrid quantum solids. [16,17]

The C-F bond has previously been used as a non-covalent interaction for materials engineering, [18] and the complex behavior of dipolar-dipolar interactions realized in crystal systems has been recognized. [19,20] Bond-dipole interactions have been observed to be more complicated [21,22] than molecular dipolar interactions, which generally do not play a pivotal role in crystal packing. [23,24] Conversely, both hydrogen and halogen bonding are reliable tools in crystal engineering for directing supramolecular self-assembly. [25–27] The variation in their steric bulk and electronegativity makes them attractive candidates in the

Author Manuscript Author Manuscript Author Manuscript Author Manuscript

manipulation of crystal packing and geometry. [28,29] C-F bond functionalization has also been extensively used in the modification of materials to improve optoelectronics, structural stability, surface activity, and processability in layered materials such as graphene and its derivatives, [30,31] 2D-perovskites, [32,33] transition metal dichalcogenides, [34,35] transition metal oxides, [36,37] metal-organic frameworks and porous coordination polymers. [38,39]

Results and Discussion

Synthesis and Purification of Fluorinated silver benzenethiolates

An overview of the synthetic scheme, precursors, and products is shown (Figure 1). For this work, we prepared silver 2-fluorobenzenethiolate, silver 3-fluorobenzenethiolate, and silver 4-fluorobenzenetholate; hereafter referred to as 2F, 3F, and 4F, respectively. We use thiorene (silver benzenethiolate), as the non-functional control example. White crystalline powders of these 2D layered compounds were recovered after the reaction of silver nitrate with the corresponding ligand in acetonitrile. Suspensions of microcrystals used for crystallographic analysis by smSFX are shown in figure 1b. Relevant bond dipole orientations of the ligands with respect to the sulfur atom are depicted (Figure 1c).

Representative scanning electron micrographs of the products 2F, 3F, and 4F products and their typical crystal habits are also shown (Figure 1d). Note the change in crystal habit from tabular in 2F, pointed-rectangular in 3F, and back to tabular in 4F. The peculiar oval-like habit of the 3F crystals shown suggests the trend towards elongation, with the curved edges implying a fast growth direction.

Ensemble Measurements of the Ligand-specific Phenomena

Microcrystals were recovered in the 3–10 μm range and in high purity. The finely powdered products were used directly for further characterization by UV-Vis, pXRD, FTIR, and thermogravimetric analysis (TGA), and these results are collected in Figure 2. The regular spacing of low-angle peaks in the p-XRD patterns (Figure 2a) is characteristic of stacked/layered materials. [9]

Thermal gravimetric analysis (TGA) experiments result in complete decomposition and loss of the organic and sulfur components, leaving a residual attributed to the silver metal with a value close to that expected from stoichiometry (Table s1, supplementary data). The 2F, 4F, and the TH control samples all share a similar decomposition temperature at 180 °C (Table s1, supplementary). The 3F is an outlier, with a higher thermal decomposition temperature of 210 °C. Because of the similarity in composition, this difference may be due to an enhancement of stability in the 3F system and might be attributable to stabilization of either the metal-sulfur bonding or to the supramolecular lattice. To explain this discrepancy, we turn to the acquisition of crystal structural data and theoretical calculations.

The vibrational spectra for each compound show a fingerprint with strong absorptions for the TH, 2F, 3F, and 4F structures. Bands highlighted in pink in figure 2c (400 – 1000 cm^{-1}) show notable differences in the vibrational modes. C-F symmetric and asymmetric stretching modes, ν(C-F) 1000 – 1400 cm^{-1}, are assigned (observed in the unhighlighted region) after inferring from literature. [40,41] Ag-S bonds are assigned (within the pink

Author Manuscript Author Manuscript Author Manuscript Author Manuscript

highlighted region) to the stretches falling below 500 cm^{-1}, with a variation in position observed across the series. The band absorption edge for all compounds fall between 3.0 eV and 3.2 eV (Figure 2d), consistent with white, crystalline solids. The intricate details about how the crystal structures obtained correspond to their IR and TGA data will be highlighted further down this report.

Structure determination of 2F, 3F, and 4F

The smSFX technique used was described in Schriber et. al. [5] Experimental metrology was refined by the process used by Brewster and coworkers. [42] *Dials.stills_process* [43,44] was used for spotfinding and indexing via the *cctbx.xfel.small_cell_process* wrapper that adds maximum clique indexing for sparse patterns. [45] TOPAS-Academic [46] was used to determine unit cells. *Cctbx.xfel.merge* was used for scaling and merging. ShelXL, [47] ShelXT, [48] Superflip, [49] Olex2, [50] and Platon [51] were used for structure solution and refinement. The data processing procedure follows steps that have been previously described[52] and are reproduced in the supporting information. Data collection and refinement statistics are shown in Table 1.

3F and **4F** were solved and refined by generally standard techniques. Structure solution was in ShelXT with the default parameters. For **4F**, the fluorophenyl group was disordered by symmetry and it was necessary to constrain the C-atom positions in a regular hexagon (AFIX 66). All non-hydrogen atomic displacement parameters were refined anisotropically with rigid-bond restraints (RIGU) on the carbon and fluorine atoms. Hydrogen atoms were placed in calculated positions and refined with riding coordinates and ADPs.

2F failed to solve in ShelXT in many repeated trials with various parameters. Our solution was obtained by running repeated trials in Superflip. For each candidate, all atoms except silver were deleted and a refinement was attempted. The solutions were evaluated for refinement stability, map quality and chemical reasonableness. The most reasonable solution was obtained in $P\bar{4}2_1c$ with two independent silver positions and one arylthiol group in the asymmetric unit. The refinement was completed with anisotropic ADPs for the heavy atoms and isotropic ADPs for carbon and fluorine. The aryl ring was constrained to a regular hexagon. Hydrogen atoms were refined with a riding model as above. We note that this structure determination for **2F** was particularly challenging, and we consider it possible that the space group is incorrect. The agreement factors (R_1 ~15%) are only slightly elevated in comparison to other structures from the same experiment, but the refinement was somewhat unstable and the atomic displacement parameters show some signs of pathology. On the other hand, we also note that in the Cambridge structural database our proposed space group, $P\bar{4}2_1c$, is the sixth most common tetragonal space group (out of 68) and the 32nd most common overall. One plausible guess is that the true symmetry is in Laue group 4/m with pseudosymmetry that approximates the extra elements .2_1. and ..*c* given here. In this scenario, our dataset would appear perfectly twinned due to the unknown orientation of individual still shots about the possible “twin elements” e.g., 2[011]. This “twinning” could explain our failure to obtain a solution in the lower Laue group, and the incorrect symmetry would explain the unstable ADPs and elevated R-factors.

Author Manuscript Author Manuscript Author Manuscript Author Manuscript

Overall, we have high confidence in our proposed structure of **2F** as a schematic depiction (sometimes called a "connectivity-quality structure"), but all details should be treated with caution. We report silver-silver distances with 2 decimal places, but it is probably impossible to meaningfully quantify the uncertainties on the measurements.

Observed Silver-silver contacts

Argentophilic Ag···Ag contacts shorter than 3.5 Å have been identified in a variety of luminescent coordination complexes [53] and in mithrene. [12] Argentophilic interactions are increasingly observed in low-dimensional materials and may play a vital role in the stabilization bonding networks. [54] The coordinative flexibility of silver atoms contribute to geometrical diversity, with a rich variety of interactions between ligands and metal centers. [55]

Argentophilic interactions are sensitive to their environments, hence, the packing of ligands in a system can influence the metallophilic contacts. [56] We observe the modification of this contact environment by comparing the three fluorine-substituted positional isomers. The overall crystal structures of the three materials are shown (Figure 3). Yunus and coworkers, through calculations at the DFT level, showed the shortest Ag···Ag interactions between 2.91 Å and 2.98 Å have the most stabilization energy value. [54] Meaningful contacts such as these have significant directional and stabilizing effects on the crystal matrix. Thus, meaningful argentophilic contacts are not observed in 2F, possibly because of the closeness of the C-F bond dipole (packing forces) to the silver metal being disruptive. The lower bond length values observed in 3F falls within the range considered to be significant. In the absence of any meaningful interactions, they may contribute to the stability of the 2D networks and 3D supramolecular frameworks. This observation agrees with the observed increased thermal stability of 3F.

Observed C–F…H interactions in 2F, 3F, and 4F crystal structures

While C-H···F hydrogen bonding is weak, this interaction can guide molecular association and alter molecular and supramolecular architectures. [57] These interactions have modest energy values ranging between of 2–20 kJ mol^{-1}, yet their effect on crystal packing is equally relevant to more typical hydrogen bonds in other crystal systems. [58,59] Here we consider the role of the fluorine position on the energy and patterns formed by C-H···F contacts. These contacts and patterns may evolve because of how the crystals pack/ assemble in the supramolecular architecture (not necessarily H-bonding).

A summary of C-H···F bond distances (intra and intermolecular) and angles in the CSD has been compiled by Hulliger and coworkers. [60] The C-H···F bond distance in 2F is 2.680 Å, while short and long intermolecular contacts [2.434 and 2.841] Å are observed in 3F. 4F also exhibits both short and long C-H···F contacts [2.658 and 2.892] Å. These contacts observed all fall within the range reported. This may not have any substantial effect on the crystal structure because they may be weak in nature due to the poor electron donating property of fluorine (F) bonded to C (sp^2). This reluctance may result from the lone pairs on fluorine conjugating with the aromatic π-electron cloud, fully utilizing its negative inductive and positive mesomeric potentials.

Author Manuscript Author Manuscript Author Manuscript Author Manuscript

Desiraju and coworkers have investigated C-H···F contacts in several fluorobenzene analogues with some showing bifurcations using IR spectroscopy. [61] They have also shown that C-F groups will prefer C-F···H interactions (hydrogen bonding) rather than F···F interactions (halogen bonding). This makes the behavior of fluorine in crystal packing different from its heavier halogen counterparts. Thus, the F···F contacts (Figure 4) observed in 3F (3.411 Å) and in 4F (3.129 Å), although they fall within the range for Fluorine-halogen bonding, they may have resulted from crystal packing considerations, with no significant stabilization effect. Using FTIR analysis, as shown in Figure 2c (blue highlighted region), we identified C-H···F contacts between 1200–1300 cm^{-1}. As seen in Table 2, bifurcations draw out more electrons from the contributing atoms, leading to weaker bonds and lower bond vibrations. With the observed C-H···F contacts in the 4F system and the bifurcated fluorine environment, this observation agrees with the lower bond vibrations observed in its IR spectrum.

Aromatic packing motifs in 2F, 3F and 4F crystal structures

Crystal structures usually pack as close as possible, with deviations being attributed to diversity in chemical makeup of crystals. Highly directional atom-specific (bonding) interactions are strong and kinetically favorable. With the incorporation of fluorine (isosteric with hydrogen) and its positioning in these supramolecules, alternative structures with different densities and packing/stacking may be realized. As hybrid structures, knowledge of how the organic groups pack is of vital interest because intermolecular interactions between crystal packing motifs can lead to the emergence of other energetically favored configurations (polymorphism). Without this information, the understanding, design, and structure prediction of this material class can be rendered challenging and tedious.

In a previous study, Hohman and coworkers have demonstrated the origin of the optoelectronic property observed in the archetype (silver benzeneselenolate), thus, attributing the new properties exhibited by members in this series to the inorganic framework was obvious from the outset. [5] As a result of the elusive nature of typical C-H···F interactions, studies done by Desiraju and coworkers in evaluating the role of C-H···F interactions in the crystal structures was key in our reconciliation of crystal structures and their thermal stabilities. [62] Additionally, Desiraju and Gavezotti drew empirical correlations between molecules and the resulting packing motifs. The common crystal packing motifs they identified now serve as a benchmark in analyzing the relationship between structure and packing. [63]

As they observed in several fluorobenzenes, we observed similar C-H···F supramolecular synthons in our three analogues (Figure 4). A linear synthon is observed in 2F, coupled with the unique 180° rotation of subsequent layers, a mesh-like arrangement of the aromatic groups present is observed. We identified their Type II synthon in the 3F analogue leading to a sandwich-herringbone arrangement of the aromatic groups. The enhanced thermal stability of 3F could also be attributed to the presence of the short C-H···F (shortest observed in the entire series) interactions and the packing motif realized in its architecture. Although the fluorine environment is bifurcated in the 4F analogue, we observed their Type I synthon which were relatively weak interactions with the herringbone arrangement of the aromatic

Author Manuscript Author Manuscript Author Manuscript Author Manuscript

group dominating. Among the members in the series, the shortest F···F contact is observed in 4F. Studies have established that Fluorine is not likely to form F···F halogen bonds because it is not easily polarizable, thus, this short contact may be due to geometric considerations (crystal packing forces).

DFT calculations

The TGA analysis reveals that the 3F crystal isomer exhibits superior thermal stability compared to the 2F and 4F counterparts. To investigate this further, we utilized a plane-wave pseudopotential formalism to calculate the energy per unit cell for all three crystals. During the computation, we relaxed all atoms and unit cell parameters while preserving the original crystal symmetry. The resulting data, presented in Table s2 (supplementary), includes the key distances that characterize the supramolecular synthons. The computed distances align with the crystallographic data and the variability in the C-H···F patterns. Specifically, the 3F system shows the shortest C-H···F distance (2.25 Å), confirming the stabilizing role of C-H···F bonds. While the DFT C-H···F distances are underestimated by approximately 7%, this is, in part, the result of an underestimation of the C-H bond lengths in the crystal structure. It is known that C-H bonds are typically underestimated by ~ 0.1 Å. The energy per unit cell per atom is lowest for the 3F system, followed by 4F and 2F, consistent with the TGA analysis.

Luminescent Polymorph of the 2F System

A polymorphic behavior is observed in the 2F case, with a second, intensely yellow product (2FY) appearing under certain conditions (Figure 5a), and this needed to first be removed. Unlike the other compounds, the powder diffraction of crude 2FY product reveals additional reflections consistent with a mixture of phases. The 2FY product is unstable to both heating and to sonication. Both post-synthetic treatments (sonication or heating) yield phase-pure 2F, yielding the diffraction pattern in Figure 5d. After purification, both the x-ray and optical signatures of the 2FY are largely absent, and all the crystals uniformly have the tabular habit (Figure 5c). Interestingly, the tabular crystal habit of the treated 2F crystals suggest elongation at the crystal edges relative to the pretreatment crystals. 2FY therefore appears to have been decomposed and added to the 2F phase crystals.

We do not include microcrystallographic analysis of the 2FY in this work as we had not isolated it before smSFX experiments, but in our synthetic follow-up efforts, we were able to obtain pure samples of 2FY. This enabled comparison of the FTIR spectra of the two phases (2FY and 2F). The spectra of the two phases is nominally indistinguishable, except for a shift in the peaks associated with the Ag-S phase as shown in (Figure s2, supplementary data). The emergence of a new diffraction peak, a 1D crystal habit, and a new optical phenomena lead us to suggest 2FY is a distinct 1D phase of 2F. This has precedence in the literature for a doubly fluorinated silver 2,6 difluorophenylselenolate, [17] so we postulate that a similar phase is accessible for the singly fluorinated species.

Author Manuscript Author Manuscript Author Manuscript Author Manuscript

Conclusion

Rational material design is a challenging problem because of the sheer diversity of possible configurations of matter. The ease of functionalization of the organic groups (R) attached to the inorganic layers in MOChas makes them interesting targets for crystal engineering. Introducing new chemical functional groups introduces two changes to the target system: the geometric demands of the group itself and the intermolecular forces it exerts on other neighbors in the crystal. This study demonstrates the potential use of C-F groups as a design tool that can be finely manipulated in the crystal engineering of hybrid systems. We characterized the energetics in the context of the crystal structures.

Methods

Chemicals used:

Silver nitrate ($AgNO_3$, ≥99.0%), acetonitrile (C_2H_3N, 99.9%), acetone (C_3H_6O, ≥99.9) and 2-fluorobenzenethiol (2-C_6H_4FSH, 97%) were purchased from Millipore Sigma. Ethanol (C_2H_5OH, 100%), 3-fluorobenzenethiol (3-C_6H_4FSH, 97.0+%), and 4-fluorobenzenethiol (4-C_6H_4FSH, 97%) were purchased from Fischer Scientific. All chemicals were used as received.

Synthesis/ Preparation of C_6H_4FSAg:

Silver precursor solution was prepared by dissolving silver nitrate (50 mg) in acetonitrile (10 mL) in a 50 mL vial. The thiol solution was prepared by combining 46 uL of X-fluorobenzenethiol (where X=2,3,4) to 10 mL acetonitrile in a beaker. The silver precursor solution was added to the thiol solution in a dropwise fashion. The resulting mixture was heated for 1 hour between 80 – 100 °C (Fig. 1a). The silver 3- and 4-fluorobenzenethiolates (3F and 4F) yield a milky – to white solid product (Fig. 1b). Silver 2-fluorobenzenethiolate yields a delicate, bright yellow solid (Fig. s1). The yellow color is attributed to a first product identified by XRD. The yellow product (2FY) is eliminated on heating or sonication to obtain a white product (2F) as shown in Fig. s1 (see supplementary). The signature of the yellow product is eliminated as observed in the diffraction pattern (Fig. s1). Silver benzenethiolate (TH) was synthesized as previously the method reported. [5]

Post Synthesis/ Purification of C_6H_4FSAg:

The precipitate was isolated by filtration. The precipitates were double washed with acetone to remove any excess precursor present. Ethanol was added to the solid obtained and sonicated for 30 min. The crystals obtained were separated from the ethanol solution by filtration and air-dried. The crystals were deposited on silicon wafer chips (5 × 5 mm) before analysis (Ted Pella, CA) by drop casting from alcohol suspension for imaging and analysis.

Instrumentation:

SEM-EDX analysis was conducted on a Phenom-World ProX Tabletop Scanning Electron Microscope. The elemental composition of the crystals were determined and quantified using the Phenom ProSuite software at 15 kV. Diffuse reflectance and absorbance ultraviolet–visible (DR UV–vis) spectra were obtained on a Shimadzu UV-2450 instrument

Author Manuscript Author Manuscript Author Manuscript Author Manuscript

from 200 nm to 800 nm. The decomposition pathway and thermal stability of the fluorinated benzenethiolates were ascertained with a TGA-Q500 Thermobalance from TA instruments. The sample was heated from 25 °C to 800 °C under a flow of nitrogen gas. Infrared spectra of the fluorinated benzenethiolates were obtained from a Thermo Fisher Nicolet 560 w/ Specac Quest ATR Accessory Spectrometer (Diamond ATR). The samples were scanned as solids from 4000 cm^{-1} – 400 cm^{-1}. The different peaks from the spectra were compared to reported values to identify the different bond vibrations in the samples. p-XRD analysis was performed with a Bruker D2 Phaser Diffractometer equipped with a high-speed linear detector (LYNXEYE) and Cu-Kα radiation (λ=1.54184 Å) at 30 kV & 10 mA. The samples were carefully packed into MTI Zero Diffraction Plate for XRD: 17.8 Dia x1.0 mm with Cavity 10 IDx0.1 mm Si Crystal for the analysis.

Density Functional Theory calculations:

All DFT calculations were performed using the plane-wave pseudopotential formalism in Quantum Espresso (10.1088/0953–8984/21/39/395502), integrated in the Schrodinger Suite 2022–4. The GGA-PBE level of theory was used with dispersion corrections (DFT-D3). Energy cutoffs of 60 Ry and 300 Ry were employed for the wavefunction and charge density, respectively. The PS Library of Dal Corso [64] was used for the application of pseudopotentials.

smSFX at SACLA:

Data collection was performed at the Experimental Hutch 3/Beamline 2 at SACLA. [65] Microcrystals were suspended in compatible carrier solvents and delivered to the X-ray interaction region by a liquid jet sample delivery system with nozzle apertures of 75 μm, 100 μm, 150 μm, and 200 μm. [66] The jet width and stability were controlled via He flow rate that ranged between 0.5 to 0.8 L/min with a steady pressure of 100 psi for the duration of the experiment. The liquid flow rate ranged between 0.1 and 0.25 mL/min. Suspensions with particle concentrations of 1 mg/mL to 4 mg/mL in 0.2% w/v aqueous surfactant solution were sonicated for 30 minutes before being aliquoted into the sample reservoir. The 30 Hz repetition rate at SACLA allows for more flexibility with jet velocity, so larger jets could be used without a loss in hit rate. We also note that the nozzle aperture and jet width used at SACLA is well-suited for samples with larger crystallite size distribution and less well-characterized samples. Lysozyme microcrystals were prepared using a standard protocol and delivered to the interaction as a calibrant for detector panel metrology.

Single-shot diffraction patterns were recorded on an Octal MPCCD detector [67] positioned ~51 mm from the interaction region with a vertical offset of 40 mm and a horizontal offset of 3 mm using the DAPHNIS platform. [68] The photon energy of the XFEL pulses was ~15.5 keV (0.8051 Å) and the beam size at the interaction region was focused to 1.2 μm using Kirkpatrick-Baez focusing mirror optics. [69] Each pulse had a duration below 10 fs [70,71] with a per-pulse energy of 0.3 m**J**. The XFEL photon flux (10^{11} photons/pulse) was not attenuated. All data collection was performed in atmospheric conditions and under room temperature.

Author Manuscript Author Manuscript Author Manuscript Author Manuscript

smSFX at LCLS:

Data collection was performed at the CXI endstation at the Linac Coherent Light Source (LCLS). [72] Microcrystals were suspended in compatible carrier solvents and delivered to the XFEL interaction region by a gas dynamic virtual nozzle (GDVN) liquid jet sample delivery system. [73] Aqueous surfactant solution (0.2–0.3% w/v) and water were used as carrier solvents, determined by their suspending power and compatibility with GDVN nozzles. The focusing He gas pressure varied from 300 to 400 psi and the liquid flow rate between 30 to 50 μL/min. Sample concentration varied between 3 mg/mL to 4 mg/mL depending on particle behavior in the suspension. Thaumatin microcrystals were prepared using a standard protocol [74] and delivered to the interaction region as a calibrant for detector panel metrology at LY65.

Single-shot diffraction patterns were recorded on a Jungfrau 4M detector [75] positioned ~59 mm and ~160 mm from the interaction region to record low resolution reflections. The photon energy of the XFEL pulses was ~18 keV (0.686 Å). The beam size at the interaction region was ~1 μm using Beryllium lens focusing optics. The pulse power and photon energy were characterized by a downstream single-shot spectrometer. [76] The repetition rate of the XFEL was 120 Hz, delivering 120 pulses per second with a pulse duration of ~30 fs and per-pulse energy of ~1–3 mJ. All data collection was performed in vacuum conditions and under room temperature. At the high photon energy of this experiment the detection efficiency of the downstream spectrometer was low, and the spectrometer background caused significant errors in the measured photon energy. Thus, we implemented a new procedure for background ("pedestal") subtraction for the downstream spectrometer. We averaged several thousand dark shots on the spectrometer and subtracted the result from all subsequent spectra.

Supplementary Material

Refer to Web version on PubMed Central for supplementary material.

Acknowledgements

The authors are grateful to the SACLA and LCLS technical and user support staff for their invaluable contribution to this effort, including Chris Kupitz at LCLS. We are also grateful for the computational support from the SACLA HPC system. XFEL experiments were conducted at SACLA with the approval of the Japan Synchrotron Radiation Research Institute (JASRI) (proposal number 2022A8066). JNH, ASB, EAS, NKS, DWP, the US Department of Energy Integrated Computational and Data Infrastructure for Scientific Discovery supported DM, VO, PK, and MA grant DE-SC0022215. EAS was supported by the Department of Energy and National Nuclear Security Administration Stewardship Science Graduate Fellowship. Research was supported by the NIH grant GM117126 to NKS. JPB and NKS were supported by the Exascale Computing Project (grant 17-SC-20-SC), a collaborative effort of the Department of Energy (DOE) Office of Science and the National Nuclear Security Administration. II was supported by the Japan Society for the Promotion of Science (KAKENHI Grants). Use of the Linac Coherent Light Source (LCLS), SLAC National Accelerator Laboratory, is supported by the U.S. Department of Energy, Office of Science, Office of Basic Energy Sciences under Contract No. DE-AC02–76SF00515. This research used resources of the National Energy Research Scientific Computing Center (NERSC), a U.S. Department of Energy Office of Science User Facility located at Lawrence Berkeley National Laboratory, operated under Contract No. DE-AC02–05CH11231.

Author Manuscript Author Manuscript Author Manuscript Author Manuscript

Data Availability Statement

Code for generating powder patterns and interfacing with GSAS-II was implemented in a DIALS/CCTBX environment, currently available from https://github.com/cctbx/cctbx-project. Crystallographic data for SFX collected for 2F, 3F, and 4F structures are available free of charge via the Cambridge Crystallographic Data Centre (CCDC).

References

[1]. Desiraju GR, Angew. Chem. Int. Ed Engl. 1995, 34,21, 2311.

[2]. Reddy DS, Ovchinnikov YE, Shishkin OV, Struchkov YT, Desiraju GR, J. Am. Chem. Soc. 1996, 118,17, 4085.

[3]. Dey A, Kirchner MT, Vangala VR, Desiraju GR, Mondal R, Howard JAK, J. Am. Chem. Soc. 2005, 127,30, 10545. [PubMed: 15631433]

[4]. Sadybekov AA, Sadybekov AV, Liu Y, Iliopoulos-Tsoutsouvas C, Huang X, Pickett J, Houser B, Patel N, Tran NK, Tong F, Zvonok N, Jain MK, Savych O, Radchenko DS, Nikas SP, Petasis NA, Moroz YS, Roth BL, Makriyannis A, Katritch V, Nature 2022, 601,7893, 452.

[5]. Schriber EA, Paley DW, Bolotovsky R, Rosenberg DJ, Sierra RG, Aquila A, Mendez D, Poitevin F, Blaschke JP, Bhowmick A, Kelly RP, Hunter M, Hayes B, Popple DC, Yeung M, Pareja-Rivera C, Lisova S, Tono K, Sugahara M, Owada S, Kuykendall T, Yao K, Schuck PJ, Solis-Ibarra D, Sauter NK, Brewster AS, Hohman JN, Nature (London) 2022, 601,7893, 360.

[6]. Riley KE, Merz KM, J Phys Chem B 2005, 109,37, 17752.

[7]. Hohman JN, Zhang P, Morin EI, Han P, Kim M, Kurland AR, McClanahan PD, Balema VP, Weiss PS, ACS nano 2009, 3,3, 527.

[8]. Mills HA, Jones CG, Anderson KP, Ready AD, Djurovich PI, Khan SI, Hohman JN, Nelson HM, Spokoyny AM, Chem. Mater. 2022, 34,15, 6933.

[9]. Paritmongkol W, Lee WS, Shcherbakov-Wu W, Ha SK, Sakurada T, Oh SJ, Tisdale WA, ACS Nano 2022, 16,2, 2054.

[10]. Yao K, Collins MS, Nell KM, Barnard ES, Borys NJ, Kuykendall T, Hohman JN, Schuck PJ, ACS Nano 2021, 15,3, 4085.

[11]. Li Yan-Zhou, Jiang Xiao-Ming, Fu Z, Qing-Qing Huang, Wang Guan-E, Deng Wei-Hua, Wang C, Li Z, Li Z, Yin Wan-Jian, Chen B, Xu G, Xu G, Nature Communications 2020, 11,1, 1.

[12]. Schriber EA, Popple DC, Yeung M, Brady MA, Corlett SA, Hohman JN, ACS applied nano materials 2018, 1,7, 3498.

[13]. Yeung M, Popple DC, Schriber EA, Teat SJ, Beavers CM, Demessence A, Kuykendall TR, Hohman JN, ACS Applied Nano Materials 2020, 3,4, 3568.

[14]. Protsailo LV, Ronald Fawcett W, Russell DD, Meyer RL, Langmuir 2002, 18,24, 9342.

[15]. Nathan Hohman J, Thomas JC, Zhao Y, Auluck HS, Kim M, Vijselaar W, Kommeren S, Kommeren S, Terfort A, Weiss PS, Journal of the American Chemical Society 2014, 136,22, 8110.

[16]. Rabl H, Myakala SN, Rath J, Fickl B, Schubert JS, Apaydin DH, Eder D, Commun Chem 2023, 6,1, 1. [PubMed: 36698004]

[17]. Sakurada T, Cho Y, Paritmongkol W, Lee WS, Wan R, Su A, Shcherbakov-Wu W, Müller P, Kulik HJ, Tisdale WA, J. Am. Chem. Soc. 2023, 145,9, 5183.

[18]. Wei F, Wei F, Feng W, Long P, Feng Y, Yiyu F, Li Y, Yu L, Advanced Science 2016, 3,7, 1500417.

[19]. Charlier A, Setton R, Charlier M, Phys. Rev. B 1997, 55,23, 15537.

[20]. Keegstra EMD, van der Mieden V, Zwikker JW, Jenneskens LW, Schouten A, Kooijman H, Veldman N, Spek AL, Chem. Mater. 1996, 8,5, 1092.

[21]. Allen FH, Baalham CA, Lommerse JPM, Raithby PR, Acta Crystallographica Section B 1998, 54,3, 320.

[22]. Lee S, Mallik AB, Fredrickson DC, Crystal Growth & Design 2004, 4,2, 279.

Author Manuscript Author Manuscript Author Manuscript Author Manuscript

[23]. Gavezzotti A, J. Phys. Chem. 1990, 94,10, 4319.

[24]. Dunitz JD, Gavezzotti A, Angewandte Chemie International Edition 2005, 44,12, 1766.

[25]. Desiraju GR, Crystal Growth & Design 2011, 11,4, 896.

[26]. Han Z, Czap G, Chiang Chi-lun, Xu C, Wagner PJ, Wei X, Wei X, Zhang Y, Zhang Y, Wu R, Ho W, Science 2017, 358,6360, 206.

[27]. Mukherjee A, Tothadi S, Desiraju GR, Accounts of Chemical Research 2014, 47,4, 2514.

[28]. Cavallo G, Metrangolo P, Milani R, Pilati T, Pilati T, Priimagi A, Resnati G, Terraneo G, Chemical Reviews 2016, 116,4, 2478.

[29]. Riley KE, Murray JS, Fanfrlík Jindřich, Řezáč Jan, Rezac J, Solá Ricardo J., Concha MC, Ramos Félix M., Politzer P, Journal of Molecular Modeling 2011, 17,12, 3309.

[30]. Jin T, Jin T, Chen J, Chen J, Wang C, Qian Y, Qian Y, Lu L, Lu L, Lu L, Journal of Materials Science 2020, 55, 12103.

[31]. Langer R, Zaoralová Dagmar, Medved M, Banáš Pavel, Błoński Piotr, Otyepka M, Journal of Physical Chemistry C 2019, 123,45, 27896.

[32]. Jeong J, Kim M, Seo J, Lu H, Ahlawat P, Mishra A, Yang Y, Hope MA, Eickemeyer FT, Kim M, Yoon YJ, Choi IW, Darwich BP, Choi SJ, Jo Y, Lee JH, Walker B, Zakeeruddin SM, Emsley L, Rothlisberger U, Hagfeldt A, Kim DS, Grätzel M, Kim JY, Nature (London) 2021, 592,7854, 381.

[33]. Wang X, Rakstys K, Rakstys K, Jack KS, Guo L, Jin H, Jin H, Lai J, Li H, Chandana Sampath KR, Chandana Sampath KR, Saghaei J, Zhang G, Burn PL, Gentle IR, Shaw PE, Nature Communications 2021, 12,1, 1.

[34]. Hight-Huf N, Pagaduan JN, Katsumata R, Emrick T, Barnes MD, J. Phys. Chem. Lett. 2022, 13,21, 4794.

[35]. Kim JT, Hyeon DS, Hanzawa K, Kanai A, Kim SY, Lee YJ, Hosono H, Bang J, Lee K, Sci Rep 2018, 8,1, 1. [PubMed: 29311619]

[36]. Emsley JW, Levason W, Reid G, Zhang W, Luca GD, Journal of Fluorine Chemistry 2017, 197, 74.

[37]. Levason W, Monzittu FM, Reid G, Zhang W, Hope EG, Journal of Fluorine Chemistry 2017, 200, 190.

[38]. Serre C, Angewandte Chemie 2012, 51, 6048. [PubMed: 22638992]

[39]. Noro Shin-ichiro, Nakamura T, NPG Asia Materials 2017, 9,9.

[40]. Li B, He T, Wang Z, Cheng Z, Liu Y, Chen T, Lai W, Wang X, Liu X, Phys Chem Chem Phys 2016, 18,26, 17495.

[41]. Wang X, Wang W, Liu Y, Ren M, Xiao H, Liu X, Anal. Chem. 2016, 88,7, 3926.

[42]. Brewster AS, Waterman DG, Parkhurst JM, Gildea RJ, Young ID, O'Riordan LJ, Yano J, Winter G, Evans G, Sauter NK, Acta Cryst D 2018, 74,9, 877.

[43]. Winter G, Waterman DG, Parkhurst JM, Brewster AS, Gildea RJ, Gerstel M, Fuentes-Montero L, Vollmar M, Michels-Clark T, Young ID, Sauter NK, Evans G, Acta Cryst D 2018, 74,2, 85.

[44]. Brewster AS, Young ID, Lyubimov A, Bhowmick A, Sauter NK, Computational Crystallography Newsletter 2019, 10, 22.

[45]. Brewster AS, Sawaya MR, Rodriguez J, Hattne J, Echols N, McFarlane HT, Cascio D, Adams PD, Eisenberg DS, Sauter NK, Acta Cryst D 2015, 71,2, 357.

[46]. Coelho AA, J Appl Cryst 2018, 51,1, 210.

[47]. Sheldrick GM, Acta Cryst C 2015, 71,1, 3.

[48]. Sheldrick GM, Acta Crystallogr A Found Adv 2015, 71,Pt 1, 3. [PubMed: 25537383]

[49]. Palatinus L, Chapuis G, J Appl Cryst 2007, 40,4, 786.

[50]. Dolomanov OV, Bourhis LJ, Gildea RJ, Howard J. a. K., Puschmann H, J Appl Cryst 2009, 42,2, 339.

[51]. Spek AL, J Appl Cryst 2003, 36,1, 7.

[52]. Aleksich M, Paley DW, Schriber EA, Linthicum W, Oklejas V, Mittan-Moreau DW, Kelly RP, Kotei PA, Ghodsi A, Sierra RG, Aquila A, Poitevin F, Blaschke JP, Vakili M, Milne CJ, Dall'Antonia F, Khakhulin D, Ardana-Lamas F, Lima F, Valerio J, Han H, Gallo T, Yousef H,

Author Manuscript Author Manuscript Author Manuscript Author Manuscript

Turkot O, Bermudez Macias IJ, Kluyver T, Schmidt P, Gelisio L, Round AR, Jiang Y, Vinci D, Uemura Y, Kloos M, Hunter M, Mancuso AP, Huey BD, Parent LR, Sauter NK, Brewster AS, Hohman JN, J. Am. Chem. Soc. 2023, 145,31, 17042.

[53]. Schmidbaur H, Schier A, Angew. Chem. Int. Ed. 2015, 54,3, 746.

[54]. Zorlu Y, Can H, Journal of Molecular Structure 2014, 1076, 629.

[55]. Caballero-Muñoz A, Guevara-Vela J, Fernández-Alarcón A, Valentín-Rodríguez MA, Flores-Álamo M, Rocha-Rinza T, Torrens H, Moreno-Alcántar G, Eur. J. Inorg. Chem. 2021, 2021,27, 2702.

[56]. Lamming G, Kolokotroni J, Harrison T, Penfold TJ, Clegg W, Waddell PG, Probert MR, Houlton A, Crystal Growth & Design 2017, 17,11, 5753.

[57]. MacDonald JC, Whitesides GM, Chem. Rev. 1994, 94,8, 2383.

[58]. Desiraju GR, Nature 2001, 412,6845, 397.

[59]. Desiraju GR, Acc. Chem. Res. 1996, 29,9, 441.

[60]. Reichenbächer K, Süss HI, Hulliger J, Chem. Soc. Rev. 2005, 34,1, 22.

[61]. Saha S, Rajput L, Joseph S, Mishra MK, Ganguly S, Desiraju GR, CrystEngComm 2015, 17,6, 1273.

[62]. Thalladi VR, Weiss H, Bläser D, Boese R, Nangia A, Desiraju GR, J. Am. Chem. Soc. 1998, 120,34, 8702.

[63]. Desiraju GR, Gavezzotti A, Acta Cryst B 1989, 45,5, 473.

[64]. Dal Corso A, Computational Materials Science 2014, 95, 337.

[65]. Yabashi M, Tanaka H, Ishikawa T, Journal of Synchrotron Radiation 2015, 22,3, 477. [PubMed: 25537581]

[66]. Tono K, High Power Laser Science and Engineering 2017, 5.

[67]. Kameshima T, Ono S, Kudo T, Ozaki K, Kirihara Y, Kobayashi K, Inubushi Y, Yabashi M, Horigome T, Holland A, Holland K, Burt D, Murao H, Hatsui T, Rev. Sci. Instrum. 2014, 85,3, 033110.

[68]. Tono K, Nango E, Sugahara M, Song C, Park J, Tanaka T, Tanaka R, Joti Y, Kameshima T, Ono S, Hatsui T, Mizohata E, Suzuki M, Shimamura T, Tanaka Y, Iwata S, Yabashi M, Journal of Synchrotron Radiation 2015, 22,3, 532. [PubMed: 25537581]

[69]. Yumoto H, Mimura H, Koyama T, Matsuyama S, Tono K, Togashi T, Inubushi Y, Sato T, Tanaka T, Kimura T, Yokoyama H, Kim J, Sano Y, Hachisu Y, Yabashi M, Ohashi H, Ohmori H, Ishikawa T, Yamauchi K, Nature Photon 2013, 7,1, 43.

[70]. Inubushi Y, Inoue I, Kim J, Nishihara A, Matsuyama S, Yumoto H, Koyama T, Tono K, Ohashi H, Yamauchi K, Yabashi M, Applied Sciences 2017, 7,6.

[71]. Inoue I, Tamasaku K, Osaka T, Inubushi Y, Yabashi M, J Synchrotron Rad 2019, 26,6, 2050.

[72]. Liang M, Williams GJ, Messerschmidt M, Seibert MM, Montanez PA, Hayes M, Milathianaki D, Aquila A, Hunter MS, Koglin JE, Schafer DW, Guillet S, Busse A, Bergan R, Olson W, Fox K, Stewart N, Curtis R, Miahnahri AA, Boutet S, Journal of Synchrotron Radiation 2015, 22, 514. [PubMed: 25931062]

[73]. DePonte DP, Weierstall U, Schmidt K, Warner J, Starodub D, Spence JCH, Doak RB, J. Phys. D: Appl. Phys. 2008, 41,19, 195505.

[74]. Nass K, Meinhart A, Barends TRM, Foucar L, Gorel A, Aquila A, Botha S, Doak RB, Koglin J, Liang M, Shoeman RL, Williams G, Boutet S, Schlichting I, IUCrJ 2016, 3,Pt 3, 180.

[75]. Leonarski F, Redford S, Mozzanica A, Lopez-Cuenca C, Panepucci E, Nass K, Ozerov D, Vera L, Olieric V, Buntschu D, Schneider R, Tinti G, Froejdh E, Diederichs K, Bunk O, Schmitt B, Wang M, Nat Methods 2018, 15,10, 799.

[76]. Zhu D, Cammarata M, Feldkamp JM, Fritz DM, Hastings JB, Lee S, Lemke HT, Robert A, Turner JL, Feng Y, Appl. Phys. Lett. 2012, 101,3, 034103.

Author Manuscript Author Manuscript Author Manuscript Author Manuscript

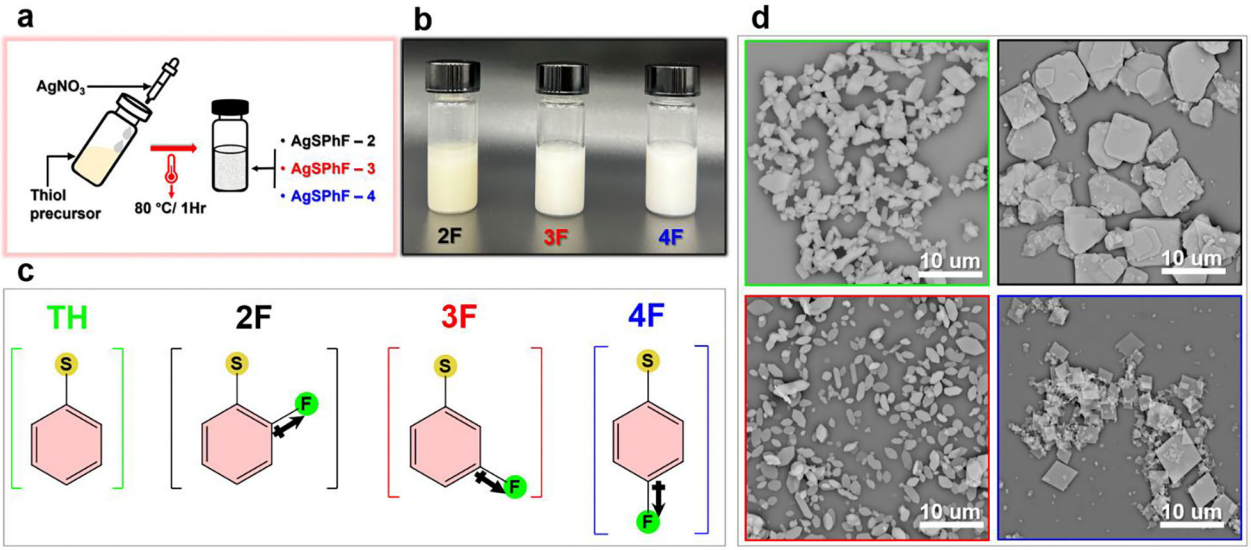

Figure 1. Synthesis

(a) schematic representation of the synthetic method used (b) cream to white colour of fluorinated silver benzenethiolate crystals in methanol (c) Thiol precursors showing the different C-F bond dipole direction in the 2, 3, and 4 positions (d) morphological variation in TH, 2F, 3F, and 4F (Neon green colour represents TH, black 2F, red 3F, and blue 4F)

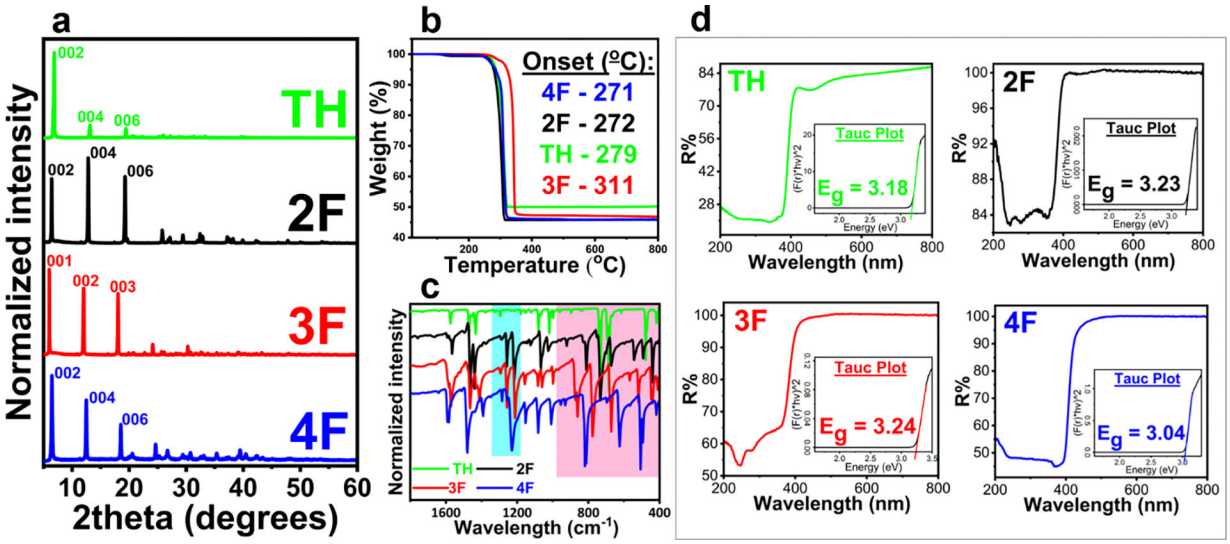

Figure 2. Secondary characterization

(a) The three evenly spaced powder XRD reflections present in all four samples are indicative of layered solids. Note the index labels are different in the 3F case because of its unique unit cell and space group. (b) 3F is distinguished in thermogravimetric analysis by a higher decomposition onset temperature. (c) IR spectra of samples. The cyan region is attributed to C-H···F contacts, pink region shows the distinct fingerprints of each structure (d) reflectance spectra and optical bandgaps of TH, 2F, 3F, and 4F.

Author Manuscript Author Manuscript Author Manuscript Author Manuscript

Author Manuscript Author Manuscript Author Manuscript Author Manuscript

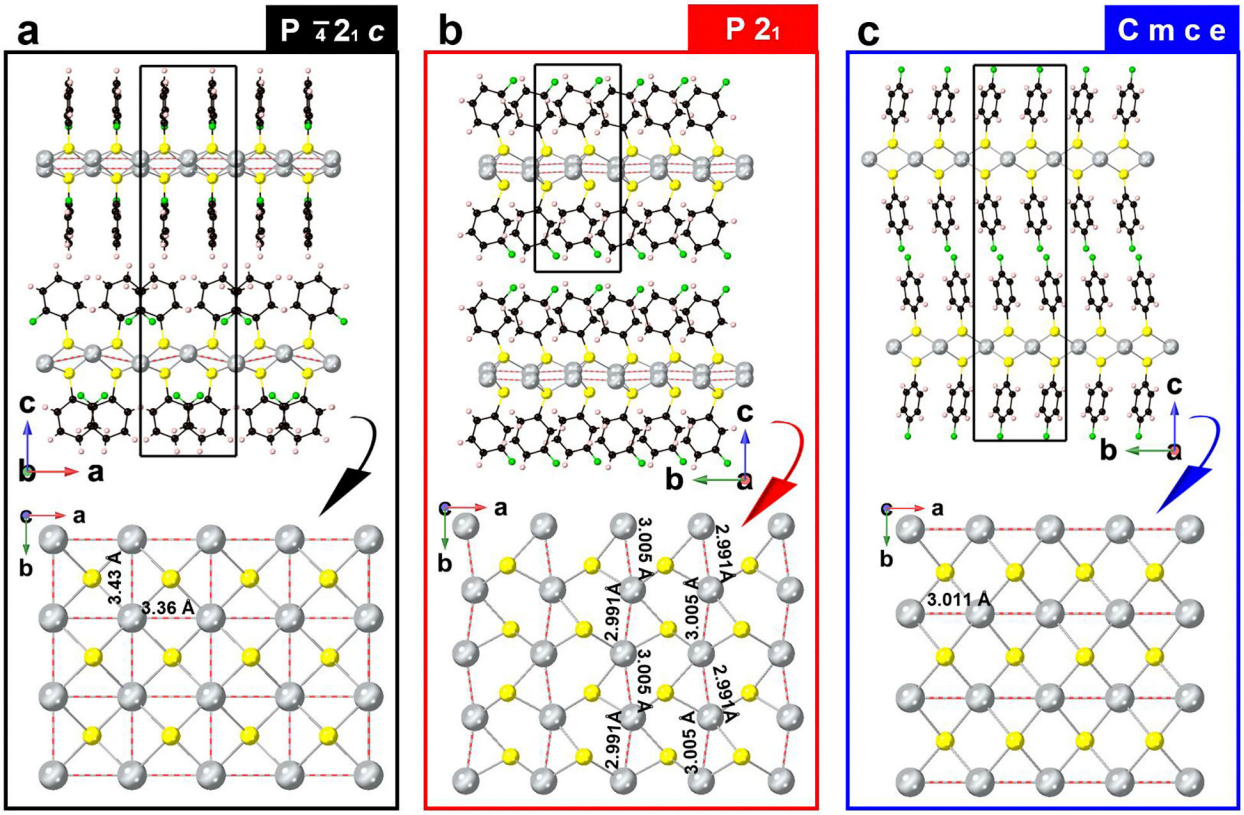

Figure 3. Crystal Structures of 2F, 3F, and 4F. Unit cells are shown in black box

(a) structure of 2F looking down the b-plane (b) structure of 3F looking down the a-plane (c) structure of 4F looking down the a-plane. A spread of possible silver-silver interactions present in 2F, 3F, and 4F is shown beneath each respective crystal structure. Note the shorter structures are shown without organic components for clarity. The Ag···Ag network in the 3F system appears to be folded. This distortion (with respect to the linear arrangement observed in 2F and 4F) may have been realized to satisfy chemical and geometric demands imposed on the supramolecular structure.

Author Manuscript Author Manuscript Author Manuscript Author Manuscript

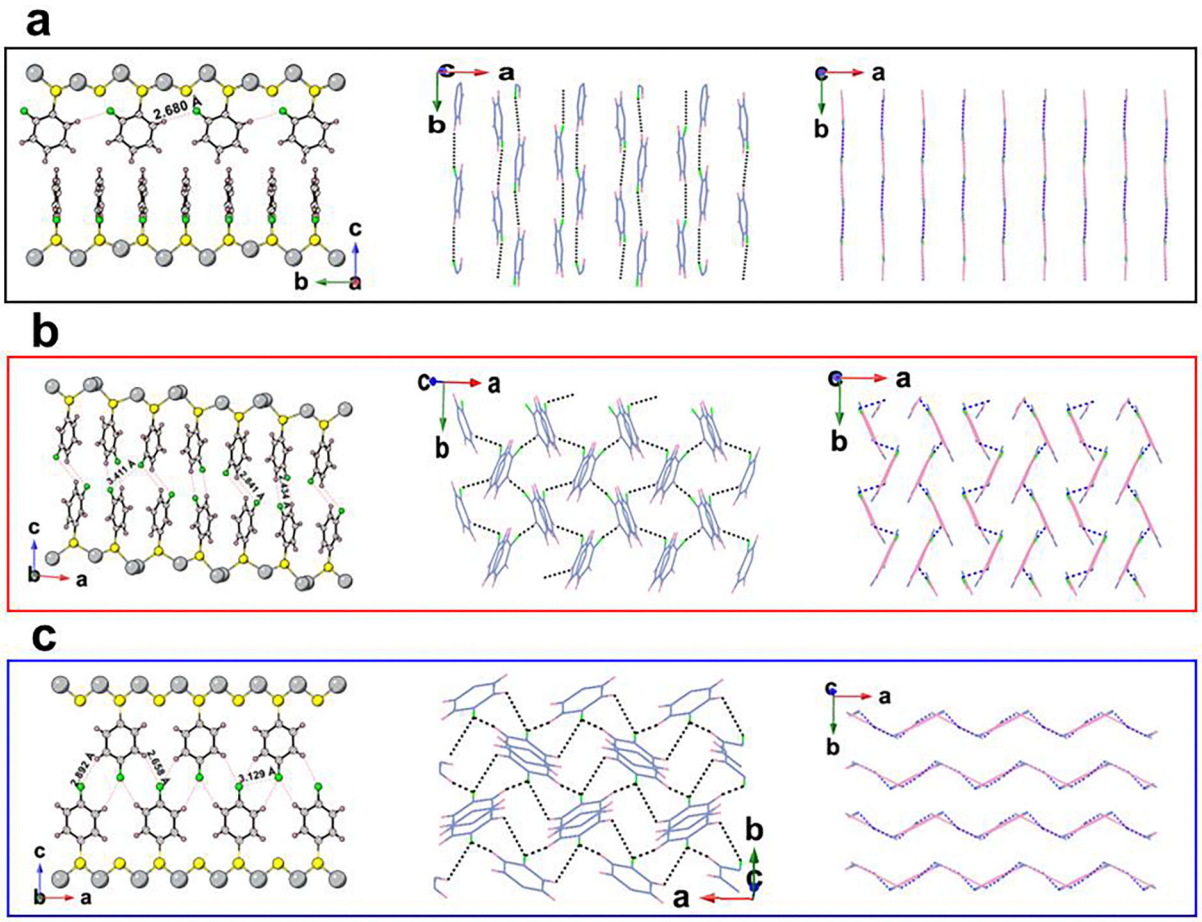

Figure 4. C-H···F synthons

(a) 2F intermolecular C-H···F contacts (2.680 Å). A linear supramolecular synthon is observed in 2F (b) Short and long intermolecular contacts [2.434 and 2.841] Å observed in 3F. A type II supramolecular synthon (catemeric) with a sandwich-herringbone arrangement of organic groups is seen (c) 4F exhibits both short and long C-H···F contacts [2.658 and 2.892] Å. Fluorine environment is bifurcated. A type I supramolecular synthon (catemeric) and a herringbone arrangement of organic groups is observed.

Author Manuscript Author Manuscript Author Manuscript Author Manuscript

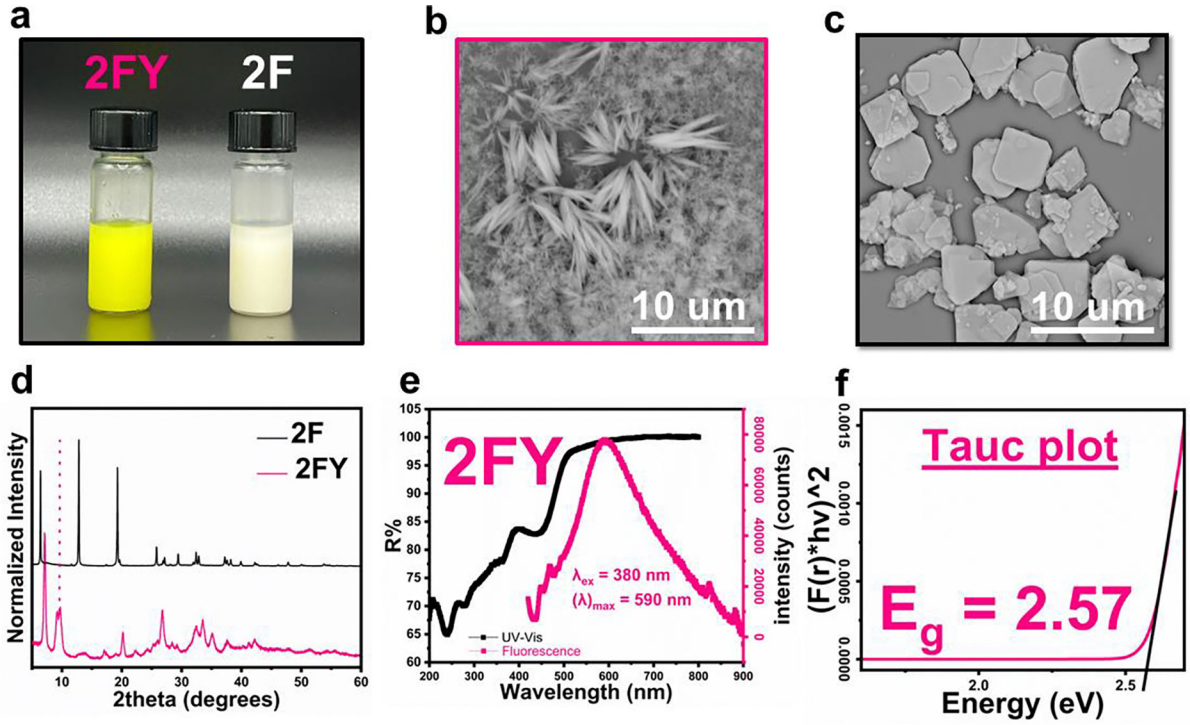

Figure 5. Luminescent polymorph

(a) Variation in 2-fluoro colour change upon sonicating or heating the 2F after synthesis. (b) and (c) show the morphological change from 2FY to 2F. (d) difference in diffraction pattern of the 2FY and 2F polymorphs. (e) luminescent property of 2FY divergent from 2F. (f) the yellow analogue (2FY) possesses a smaller bandgap.

Author Manuscript Author Manuscript Author Manuscript Author Manuscript

Table 1

Data collection and refinement statistics

Compound	**2F**	**3F**	**4F**
Formula	$AgSC_6H_4F$	$AgSC_6H_4F$	$AgSC_6H_4F$
MW	235.02	235.02	235.02
Space group	$P\bar{4}2_1c$	$P2_1$	*Cmce*
***a* (Å)**	6.717	7.371	6.023
***b* (Å)**	6.717	5.935	7.262
***c* (Å)**	27.443	14.887	29.520
α (°)	90	90	90
β (°)	90	95.45	90
γ (°)	90	90	90
V (Å^3)	1238.1	648.3	1291.2
Z	8	4	8
ρ_{calc} (g cm^{-3})	2.522	2.408	2.418
XFEL source	SACLA	LCLS	LCLS
λ (Å)	0.79887	0.69465	0.69458
T (K)	298	298	298
d_{min}(Å)	0.83	0.83	0.83
μ(mm^1)	4.845	3.159	3.168
Frames	520000	308401	980726
Crystals	2644	6283	6414
Time (min)	289	43	136
Data	679	1305	657
Restraints	1	91	46
Parameters	37	163	64
R_1(obs) (%)	14.6	9.05	9.63
R_1(all) (%)	22.6	9.78	13.3
S	1.46	1.13	1.11
Peak, hole (e$^-$ Å^{-3})	1.58, −1.44	1.81, −1.03	.72, −.60

Author Manuscript Author Manuscript Author Manuscript Author Manuscript

Table 2

Possible C-H···F contacts confirmed with IR data.

A bifurcated fluorine environment is observed in the 4-fluoro analogue.

IR characteristics of samples			
Sample	**C-H environment**	**F environment**	**C-F…H (cm^{-1})**
2F	**Non-bifurcated**	**Non-bifurcated**	**1290, 1260, 1218**
3F	**Non-bifurcated**	**Non-bifurcated**	**1295, 1260, 1214**
4F	**Non-bifurcated**	**Bifurcated**	**1284, 1259, 1231**